Available online at www.sciencedirect.com
ScienceDirect
Comput. Methods Appl. Mech. Engrg. 303 (2016) 163–184
Computer methods in applied mechanics and engineering
www.elsevier.com/locate/cma

A numerical study of void coalescence and fracture in nonlinear elasticity

Duvan Henao[a], Carlos Mora-Corral[b], Xianmin Xu[c,*]

[a] *Faculty of Mathematics, Pontificia Universidad Católica de Chile, Vicuña Mackenna 4860, Macul, Santiago, Chile*
[b] *Department of Mathematics, Faculty of Sciences, Universidad Autónoma de Madrid, E-28049, Madrid, Spain*
[c] *LSEC, Institute of Computational Mathematics and Scientific/Engineering Computing, NCMIS, Chinese Academy of Sciences, Beijing 100190, China*

Received 15 January 2015; received in revised form 14 January 2016; accepted 16 January 2016
Available online 27 January 2016

Abstract

We present a numerical implementation of a model for void coalescence and fracture in nonlinear elasticity. The model is similar to the Ambrosio–Tortorelli regularization of the standard free-discontinuity variational model for quasistatic brittle fracture. The main change is the introduction of a nonlinear polyconvex energy that allows for cavitation. This change requires new analytic and numerical techniques. We propose a numerical method based on alternating directional minimization and a stabilized Crouzeix–Raviart finite element discretization. The method is used in several experiments, including void coalescence, void creation under tensile stress, failure in perfect materials and in materials with hard inclusions. The experimental results show the ability of the model and the numerical method to study different failure mechanisms in rubber-like materials.
© 2016 Elsevier B.V. All rights reserved.

Keywords: Cavitation; Fracture; Void coalescence; Nonlinear elasticity; Γ-convergence; Ambrosio–Tortorelli approximation

1. Introduction

Cavitation, which consists in the sudden appearance of cavities under sufficiently large tensions, is an important failure phenomenon in rubber-like solids and ductile metals. For a better description of this instability and of the wide range of situations where it occurs, we refer the reader to the seminal experiments of Gent and Lindley [1] in short rubber cylinders, and to the observations of cavitation in other elastomers (see [2,3] and the references therein), in gels [4], in elastomer networks [5,6], in elastomers reinforced by hard inclusions or fibres [7,8], and in titanium alloys (where the nucleation of cracks is due to the rapid enlargement of the cavities and their subsequent coalescence, [9]).

Cavitation has been modelled and analysed under two approaches. One is based on the hypothesis that cavities grow from pre-existing micro-defects in the material [2]. Under this assumption, Gent and Lindley [1] analysed the critical load at which cavitation occurs in a spherical void in an infinite extension of a neo-Hookean material, obtaining a very good agreement with the experiments. The other approach, firstly studied by Ball [10], does not rely on the

* Corresponding author.
E-mail addresses: dhenao@mat.puc.cl (D. Henao), carlos.mora@uam.es (C. Mora-Corral), xmxu@lsec.cc.ac.cn (X. Xu).

http://dx.doi.org/10.1016/j.cma.2016.01.012
0045-7825/© 2016 Elsevier B.V. All rights reserved.

assumption of the existence of material defects. By formulating the analysis in terms of an energy minimization problem in a space of admissible deformations allowing for the existence of point discontinuities, he proved the existence of a well-defined critical load at which a family of deformations creating a cavity at the centre of a ball becomes energetically more favourable and bifurcates from the homogeneous solution of the equilibrium equations. The two approaches are proved to be equivalent if one assumes that the cavities can open only at some fixed points in perfect materials [11,12]. Further studies of these two models are developed in [13–18], among others.

In comparison with the relatively extensive mathematical analyses and experimental results, the numerical studies for cavitation using elasticity theory are insufficient. There are some key difficulties in the cavitation problem from the numerical point of view. Firstly, the nonlinear elastic energy functional proposed by Ball exhibits the well-known Lavrentiev phenomenon [19]: the minimizer of the energy functional in $W^{1,\infty}$ is different from that in $W^{1,p}$ with $p < n$ (here n is the dimension of the space). While the latter corresponds to a cavitation solution, the standard finite element method can only approximate the former. Although there are some numerical methods developed to deal with the Lavrentiev phenomenon [20–24], none of them are suitable for the cavitation problem. On the other hand, if one assumes that there are pre-existing micro-holes, the current numerical methods work only when one knows the position of those defects [25–34], or when an arbitrarily large number of micro-holes is spread over the sample [35–39]. It is a hard problem for a numerical method based on nonlinear elasticity to find automatically the location of the cavities [40]. In fact, in the context of nonlinear elasticity, this is, as far as we know, the first work allowing for void coalescence. Existing numerical simulations for void coalescence use elastoplasticity [35,41,32], crystal plasticity [42,27,28,43], damage models [36], molecular dynamics [44–46] or atomistic simulations [47]. See [48] for a review of several models of void nucleation, growth and coalescence. Our work has the advantage that neither the location, nor the number, nor the shape of cavities is specified a priori; instead, they are part of the unknowns in our free-discontinuity model.

A free-discontinuity model for cavitation and fracture in nonlinear elasticity was analysed in [16,17], bringing together the approaches of [13] for cavitation and [49] for fracture. The model is static and based on energy minimization. In [50] we proposed a phase-field approximation (in the sense of Γ-convergence) of that model, inspired in the Ambrosio–Tortorelli [51] type of approximation for fracture [52–54], where the phase-field function captures the crack path and makes the problem suitable for a numerical discretization. In this paper, we propose a numerical method for [50] which combines the alternating direction minimizing approach with a stabilized Crouzeix–Raviart finite element discretization of the energy; it is easy to implement and robust for various numerical examples. We also carry out a series of experiments which show the capability of the model to accurately capture the formation of voids and the initiation of fracture in elastomers, as well as the potential it has to enhance and complement the existing models for ductile fracture: the classical models [55,56,9] based on continuum damage mechanics; the multiscale approach of Reina, Li, Weinberg and Ortiz [57] based on a space-filling assemblage of hollow spheres; and the recent works by Fokoua, Conti and Ortiz [58,59] where a sublinear energy is regularized with a non-local term coming from strain-gradient micro plasticity (see also [60]).

The structure of the paper is as follows. In Section 2 we introduce the continuous model and its phase-field approximation. In Section 3 we explain the numerical method. Sections 4–7 present the numerical experiments. In materials with micro-holes (Section 4), the cavities grow dramatically under sufficiently large tensions and then fracture occurs. In Section 5 we study the initiation of fracture in perfect materials. In Sections 6 and 7 we simulate Gent and Lindley's [1] experiments of void nucleation in short rubber cylinders and study the internal rupture of materials with hard inclusions. In Section 8 we present some simulations which aim to shed some light on how the initiation of fracture is affected by the growth of the stored-energy function at infinity. Finally, conclusions and outlooks are given in Section 9, including a comparison of our approach with the recent work by Lefèvre, Ravi-Chandar and Lopez-Pamies [39].

2. A phase-field approximation for void coalescence and fracture

2.1. The energy model for cavitation

In nonlinear elasticity [61], the deformation of an elastic body is determined by minimization of the total energy

$$I^{el}(\mathbf{u}) := \int_{\Omega} W(\nabla \mathbf{u})\, \mathrm{d}\mathbf{x}, \tag{2.1}$$

where $\Omega \subset \mathbb{R}^n$ ($n = 2, 3$) is the reference domain, $\mathbf{u} : \Omega \to \mathbb{R}^n$ is the deformation function, $\nabla \mathbf{u}$ its gradient and W is the nonlinear elastic energy density. A typical example is

$$W(\mathbf{F}) = \frac{\mu}{p}|\mathbf{F}|^p + f(\det \mathbf{F}), \tag{2.2}$$

where $\mathbf{F}$ is the deformation gradient, $|\cdot|$ denotes the Frobenius norm of a matrix, $p > 1$ is the growth exponent, $\mu > 0$ is the shear modulus and $f : (0, \infty) \to \mathbb{R}$ is a given convex function characterizing the compressibility of the material. For this type of energy density, Ball [10] showed that, under some assumptions, notably $n - 1 < p < n$ and

$$\lim_{s \to 0^+} f(s) = \lim_{s \to \infty} \frac{f(s)}{s} = \infty, \tag{2.3}$$

the functional (2.1) can have a singular minimizer, which corresponds to cavitation in rubber-like materials. The existence of singular minimizers in the Sobolev space $W^{1,p}(\Omega)$ is further discussed in [13,14,12].

It is known that the energy model for cavitation exhibits the Lavrentiev phenomenon, i.e., the minimum of the energy functional in $W^{1,\infty}(\Omega)$ is strictly larger than that in $W^{1,p}(\Omega)$, which makes the problem difficult to solve numerically (see, e.g., [19,62]). A way to overcome this was proposed by Sivaloganathan, Spector and Tilakraj [11]: their model assumes that there are some pre-existing micro-holes in the material. In this way, the domain under consideration is

$$\Omega_\delta := \Omega \setminus \Big(\bigcup_i B(\mathbf{a}_i, \delta) \Big), \tag{2.4}$$

where $B(\mathbf{a}_i, \delta)$ is a spherical hole centred at $\mathbf{a}_i$ with small radius $\delta > 0$. The corresponding energy functional is

$$I_\delta^{el}(\mathbf{u}) := \int_{\Omega_\delta} W(\nabla \mathbf{u}) \, d\mathbf{x}. \tag{2.5}$$

Moreover, the deformation is assumed not to create any other hole apart from $\mathbf{a}_i$. This is expressed mathematically as $\operatorname{Det} \nabla \mathbf{u} = \det \nabla \mathbf{u}$ in Ω_δ, i.e., the distributional determinant $\operatorname{Det} \nabla \mathbf{u}$ equals the pointwise determinant $\det \nabla \mathbf{u}$ (see, e.g., [61,63,13]). This model has been implemented numerically in [29,30].

2.2. *Mumford–Shah functional for fracture and its approximation*

Francfort and Marigo [49] added a Mumford–Shah [64] term to the linear elastic energy to study the propagation of brittle fracture. The nonlinear version of their functional is

$$I^{MS}(\mathbf{u}) := \int_\Omega W(\nabla \mathbf{u}) \, d\mathbf{x} + \alpha \mathcal{H}^{n-1}(J_\mathbf{u}), \tag{2.6}$$

where $\mathcal{H}^{n-1}(J_\mathbf{u})$ is the $(n-1)$-dimensional area of the jump set $J_\mathbf{u}$ of $\mathbf{u}$, and $\alpha > 0$ is a parameter representing the material fracture toughness. We minimize the problem in the space $SBV(\Omega)$ of functions of special bounded variation [65]. The second term penalizes the formation of cracks, which is consistent with Griffith's [66] theory of fracture.

The Mumford–Shah model (2.6) is difficult to solve numerically because of the sharp interface $J_\mathbf{u}$. Instead, we consider, as in [52–54], an Ambrosio–Tortorelli [51] type of approximation for the functional I^{MS} using a diffuse interface model. We introduce a smooth function z that indicates healthy material if $z \simeq 1$ and damaged material if $z \simeq 0$. The functional (2.6) is approximated by

$$I(\mathbf{u}, z) := \int_\Omega (z^2 + \eta) \, W(\nabla \mathbf{u}) \, d\mathbf{x} + \alpha \int_\Omega \left(\varepsilon |\nabla z|^2 + \frac{(z-1)^2}{4\varepsilon} \right) d\mathbf{x}. \tag{2.7}$$

Here $\eta, \varepsilon > 0$ are small parameters: ε corresponds approximately to the width of the diffuse interface that approximates the sharp discontinuity $J_\mathbf{u}$; the parameter η, which is assumed to be much smaller than ε, is added

to preserve the ellipticity of the analytical problem (and the stability of the numerical method) in the damaged regions where z becomes close to zero. The second term in (2.7) is an approximation of $\mathcal{H}^{n-1}(J_{\mathbf{u}})$.

The boundary conditions are as follows. We decompose the boundary $\partial\Omega$ as a disjoint union of the Dirichlet part $\partial_D\Omega$ and the Neumann part $\partial_N\Omega$; we allow $\partial_N\Omega$ to be empty. We fix a boundary value $\mathbf{u}_D : \partial_D\Omega \to \mathbb{R}^n$ and prescribe $\mathbf{u}(\mathbf{x}) = \mathbf{u}_D(\mathbf{x})$ and $z(\mathbf{x}) = 1$ on $\partial_D\Omega$, which means that we do not allow the Dirichlet boundary to fracture. On $\partial_N\Omega$, we choose traction-free boundary conditions for $\mathbf{u}$, and $z = 0$. We choose this condition on z only for consistency with the convergence analysis of [50], where it was assumed for technical convenience (in order to prove more easily one of the intermediate claims). The more intuitive homogeneous Neumann boundary condition on z can also be imposed on $\partial_N\Omega$; nevertheless, this does not make a real difference: it was proved in [50] that as $\eta, \varepsilon \to 0$ the choice $z = 0$ leads to an energy that differs from I^{MS} only by an additive constant (namely, $\frac{1}{2}\mathcal{H}^{n-1}(\partial_N\Omega)$). For simplicity, we do not consider the homogeneous Neumann condition for z in this paper, although it seems more physical.

Declare the admissible set for $\mathbf{u}$ to be

$$\mathbf{U} := \{\mathbf{u} \in W^{1,p}(\Omega)^n : \ \operatorname{Det}\nabla\mathbf{u} = \det\nabla\mathbf{u},\ \mathbf{u}(\mathbf{x}) = \mathbf{u}_0(\mathbf{x}) \text{ on } \partial_D\Omega\}.$$

The functional space for z is

$$V := \{z \in W^{1,2}(\Omega) : \ z(\mathbf{x}) = 1 \text{ on } \partial_D\Omega,\ z(\mathbf{x}) = 0 \text{ on } \partial_N\Omega\}.$$

It is not necessary to impose the constraint $0 \le z \le 1$ in V since it can be shown [54] that minimizers always satisfy that condition. The approximation problem considered in this paper is given as

$$\min_{\mathbf{u}\in\mathbf{U},\, z\in V} I(\mathbf{u}, z). \tag{2.8}$$

2.3. Γ-convergence results

When the energy density W is quadratic or quasiconvex, the Γ-convergence of (2.7) to (2.6) as $\eta \ll \varepsilon \to 0$ was studied in [51,67,52,68,69]. The adaptation of those results to the polyconvex functional (2.2) with the growth (2.3) and $p < n$ (as is crucial in the theory of cavitation, and as considered in this paper), was analysed in [50]: we proved that a suitable variant of (2.7), namely,

$$\begin{aligned}\bar{I}_{\varepsilon,\eta}(\mathbf{u}, z, w) := &\int_\Omega (z^2+\eta)\, W(\nabla\mathbf{u})\,\mathrm{d}\mathbf{x} + \alpha\int_\Omega\left(\varepsilon^{q-1}|\nabla z|^q + \frac{(z-1)^{q'}}{4\varepsilon}\right)\mathrm{d}\mathbf{x}\\ &+ 6\beta\int_{\mathbf{u}(\Omega)}\left(\varepsilon^{q-1}|\nabla w|^q + \frac{w^{q'}(w-1)^{q'}}{4\varepsilon}\right)\mathrm{d}\mathbf{y}.\end{aligned} \tag{2.9}$$

Γ-converges to

$$\bar{I}(\mathbf{u}) := \int_\Omega W(\nabla\mathbf{u})\,\mathrm{d}\mathbf{x} + \alpha\left[\mathcal{H}^{n-1}(J_{\mathbf{u}}) + \mathcal{H}^{n-1}(\{\mathbf{x}\in\partial_D\Omega : \mathbf{u}\neq\mathbf{u}_0\}) + \frac{1}{2}\mathcal{H}^{n-1}(\partial_N\Omega)\right] + \beta\bar{\mathcal{E}}(\mathbf{u}). \tag{2.10}$$

Here w is an auxiliary scalar function, which essentially can be thought to be $w(\mathbf{y}) = z(\mathbf{u}^{-1}(\mathbf{y}))$. Also, $q > n$ and $\bar{\mathcal{E}}(\mathbf{u})$ is a surface energy accounting for the stretching of all surfaces of the body (including the created cavities and fractures): it measures the area of those surfaces as they are seen in the deformed configuration [16,17,50]. The presence of the auxiliary function w makes the last integral of (2.9) converge to the surface energy $\bar{\mathcal{E}}(\mathbf{u})$. As explained in Section 2.2, the term $\frac{1}{2}\mathcal{H}^{n-1}(\partial_N\Omega)$ appears more for technical reasons (due to the boundary condition $z = 0$ on $\partial_N\Omega$). The last term in (2.9) is essential in the analysis of [50] to control the convergence of the determinant of the deformation gradient. Nevertheless, it has turned out not to make a qualitative difference in the numerical simulations (expect for the fact that the created cavities and cracks are somewhat more smooth and rounded, since $\bar{\mathcal{E}}(\mathbf{u})$ corresponds essentially to a surface tension). We have therefore decided not to include it in this numerical study, for simplicity. Besides, we have not taken the restriction $q > n$ into account and set $q = 2$.

3. The numerical method

3.1. Alternating minimization and gradient flow

The functional I of (2.7) has two variables: $\mathbf{u}$ and z. Numerically, it is convenient to minimize I by alternating-direction methods [52,54].

Algorithm 1.

- Step 1. Fix a tolerance $TOL > 0$ (in our experiments we chose $TOL = 10^{-5}$). Set $k = 0$ and some initial functions $\mathbf{u}^0$ and z^0.
- Step 2. Given z^k, find

$$\mathbf{u}^{k+1} = \arg\min_{\mathbf{u}\in\mathbf{U}} I(\mathbf{u}, z^k). \tag{3.1}$$

- Step 3. Given $\mathbf{u}^{k+1}$, find

$$z^{k+1} = \arg\min_{z\in V} I(\mathbf{u}^{k+1}, z). \tag{3.2}$$

- Step 4. If $\|z^{k+1} - z^k\| \leq TOL$, stop; otherwise, set $k = k + 1$ and go back to Step 2.

Sub-problem (3.1) is a pure cavitation problem, as studied by [29], whereas sub-problem (3.2) corresponds to a linear elliptic equation.

To solve (3.1) and (3.2), we compute the Gâteaux derivative of I. In truth, we only perform a formal calculation, since a rigorous one is out of the scope of this work. Defining

$$\mathbf{U}_0 := \{\mathbf{u} \in W^{1,p}(\Omega)^n : \mathbf{u}(\mathbf{x}) = \mathbf{0} \text{ on } \partial_D\Omega\}$$

and

$$V_0 := \{z \in W^{1,2}(\Omega) : z(\mathbf{x}) = 0 \text{ on } \partial\Omega\},$$

one can easily find that, formally, the Gâteaux derivative of I at $(\mathbf{u}, z) \in \mathbf{U} \times V$ in the direction $(\mathbf{v}, \phi) \in \mathbf{U}_0 \times V_0$ is

$$I'(\mathbf{u}, z; \mathbf{v}, \phi) = a(z; \mathbf{u}, \mathbf{v}) + b(\mathbf{u}; z, \phi), \tag{3.3}$$

with

$$a(z; \mathbf{u}, \mathbf{v}) := \int_\Omega (z^2 + \eta)\, \partial_{\mathbf{F}} W(\nabla\mathbf{u}) : \nabla\mathbf{v}\, \mathrm{d}\mathbf{x},$$

$$b(\mathbf{u}; z, \phi) := 2\int_\Omega \left[W(\nabla\mathbf{u})\, z\, \phi + \alpha\left(\varepsilon\, \nabla z \cdot \nabla\phi + \frac{(z-1)\phi}{4\varepsilon}\right)\right] \mathrm{d}\mathbf{x}.$$

There are two difficulties in making the above process rigorous. One is to commute the derivates with the integral, which is unclear because of condition (2.3). The second is to tackle the nonlinear constraint $\mathrm{Det}\, D\mathbf{u} = \det D\mathbf{u}$, which we ignore for this formal calculation.

Sub-problem (3.2) is equivalent to finding $z^{k+1} \in V$ such that

$$b(\mathbf{u}^{k+1}; z^{k+1}, \phi) = 0, \quad \forall\phi \in V_0. \tag{3.4}$$

Sub-problem (3.1), on the other hand, is a nonlinear nonconvex minimization problem. We have chosen the following gradient flow method to solve it numerically: find an evolution of $\mathbf{u} \in \mathbf{U}$ such that

$$\begin{aligned} &(\nabla\mathbf{u}_t, \nabla\mathbf{v}) = -a(z^k; \mathbf{u}, \mathbf{v}), \quad \forall\mathbf{v} \in \mathbf{U}_0,\ t > 0,\\ &\mathbf{u}(0) = \mathbf{u}^k. \end{aligned} \tag{3.5}$$

The bracket in (3.5) indicates inner product in L^2, and $\mathbf{u}_t$ denotes the derivative of $\mathbf{u}$ with respect to t. A formal calculation shows that $\mathbf{u}_t \in \mathbf{U}_0$; using this, we find that

$$\frac{\mathrm{d}I(\mathbf{u}, z^k)}{\mathrm{d}t} = a(z^k; \mathbf{u}, \mathbf{u}_t) = -\int_\Omega \nabla\mathbf{u}_t : \nabla\mathbf{u}_t\, \mathrm{d}\mathbf{x} \leq 0,$$

so this gradient flow method has the familiar energy decay property.

3.2. Non-conforming finite element approximation and its stabilization

For the space discretization, we use the Crouzeix–Raviart (C–R) finite element method [70] to approximate the energy functional. The method, which has been successfully used [29] to compute the cavitation problem, is able to approximate efficiently deformations with large strains, as those that often appear in rubber-like materials, especially when cavitation occurs.

We now describe our method. In the rest of the paper, $n = 2$. In most of our experiments, the width ε of the diffuse interface that replaces the sharp discontinuities associated to cavitation and fracture is of the order of $\varepsilon \sim 10^{-3}$ diam Ω; the stabilization parameter η is of the order of $\eta \sim 10^{-7}$ diam Ω. We triangulate the domain using a *regular* triangular mesh $\mathcal{T}_h$ (in the sense of Ciarlet [71]). We have found that a triangulation in which $h \sim \frac{\varepsilon}{10}$, where h denotes the diameter of the smallest elements, is sufficiently fine to accurately resolve the interface.

Denote by $\mathcal{E}$ the set of all edges in $\mathcal{T}_h$, and by $\mathcal{M}$ the set of middle points of the edges. The C–R finite element space is given by

$$X_h := \{v_h : \Omega \to \mathbb{R} : v_h \text{ is continuous on } \mathcal{M} \text{ and } v_h|_T \text{ is affine for each } T \in \mathcal{T}_h\}.$$

The finite element space for the displacement function is given as

$$\mathbf{U}_h := \{\mathbf{u}_h \in (X_h)^2 : \mathbf{u}_h(\mathbf{x}_i) = \mathbf{u}_D(\mathbf{x}_i)\ \forall \mathbf{x}_i \in \mathcal{M} \cap \partial_D \Omega\}.$$

Likewise, $\mathbf{U}_{h,0}$ is defined as the set of $\mathbf{u}_h \in (X_h)^2$ such that $\mathbf{u}_h = \mathbf{0}$ in $\mathcal{M} \cap \partial_D \Omega$. The C–R element space for the damage variable z is given by

$$V_h := \{z_h \in X_h : z_h(\mathbf{x}_i) = 1\ \forall \mathbf{x}_i \in \mathcal{M} \cap \partial_D \Omega,\ z_h(\mathbf{x}_i) = 0\ \forall \mathbf{x}_i \in \mathcal{M} \cap \partial_N \Omega\},$$

whereas $V_{h,0}$ set of $z_h \in X_h$ such that $z_h = 0$ on $\mathcal{M} \cap \partial \Omega$.

The discrete energy functional I_h is just the restriction of I to $\mathbf{U}_h \times V_h$. It was observed in [29] that the C–R finite element method is unstable for the cavitation problem. This is solved, as in [29], by adding a stabilization term to the discrete energy functional I_h. Accordingly, we define

$$I_h^{st}(\mathbf{u}_h, z_h) := I_h(\mathbf{u}_h, z_h) + C \sum_{E \in \mathcal{E}} h_E^{\gamma} \int_E (z_h^2 + \eta)\, |[\mathbf{u}_h]|^2 \, \mathrm{d}s \tag{3.6}$$

where $C > 0$ and $\gamma \in \mathbb{R}$ are parameters, h_E is the length of the side E, and $[\cdot]$ denotes the jump of a given quantity across the corresponding side. Thus, $|[\mathbf{u}_h]|^2$ penalizes the discontinuity of the discrete deformation $\mathbf{u}_h$, and, in particular, it vanishes when $\mathbf{u}_h$ is continuous across the edge. Note that the term $(z_h^2 + \eta)$ multiplies $|[\mathbf{u}_h]|^2$: the reason is that our model allows for fracture, so we are not to penalize jumps in $\mathbf{u}_h$ when there is fracture, i.e., when $z_h \simeq 0$.

The choice of the exponent γ is delicate. A proper study, outside of the scope of this work, should be accompanied with a joint scaling analysis of the parameters ε and h. We just mention here that there are two natural choices for γ, namely, 0 and -2. Indeed, when $\gamma = 0$, the term

$$C \sum_{E \in \mathcal{E}} h_E^{\gamma} \int_E |[\mathbf{u}_h]|^2 \, \mathrm{d}s$$

is the usual penalty term for the jump of the function $\mathbf{u}_h$, as in the standard discontinuous Galerkin method. As for $\gamma = -2$, we first make the following elementary observation. For each edge E, let $\mathbf{x}_0$ be its middle point. As $[\mathbf{u}_h](\mathbf{x}_0) = 0$, it is easy to see that $[\mathbf{u}_h](\mathbf{x}) = [\nabla \mathbf{u}_h(\mathbf{x}_0)](\mathbf{x} - \mathbf{x}_0)$ for $\mathbf{x} \in E$. Thus,

$$h_E^{-2} \int_E |[\mathbf{u}_h]|^2 \, \mathrm{d}s = \frac{1}{12} \int_E |[\nabla \mathbf{u}_h\, \mathbf{s}]|^2 \, \mathrm{d}s, \tag{3.7}$$

where $\mathbf{s}$ is the unit vector parallel to E. Thus, (3.7) corresponds to a penalty of the jumps of the tangential derivatives of $\mathbf{u}_h$ on the edges, as done in [29].

For a given mesh, one can cure the instability by adjusting the values of γ and C. According to our numerical experiments, if the mesh is not extremely fine, one can choose $\gamma = 0$ and a very large C (e.g., $C = 2500$). Alternatively, one can also choose $\gamma = -2$ and a small C (e.g., $C = 0.2$). In the simulations in this paper, we

set $\gamma = 0$ and $C = 2500$ in most cases. Experiments show that such a choice prevents the instability and makes the gradient flow faster than any other value of γ between -2 and 0.

3.3. The algorithm

The discrete problem corresponding to (2.8) is to minimize the energy functional in the finite element space $\mathbf{U}_h \times V_h$:

$$\min_{\mathbf{u}_h \in \mathbf{U}_h,\, z_h \in V_h} I_h^{st}(\mathbf{u}_h, z_h). \tag{3.8}$$

We will solve the problem by an alternating-direction method, as in Algorithm 1. For this, we need to solve two discrete minimization problems similar to (3.1) and (3.2). Accordingly, we compute the Gâteaux derivative of I_h^{st}. As in (3.3), we have, for $\mathbf{u}_h \in \mathbf{U}_h$, $z_h \in V_h$, $\mathbf{v}_h \in \mathbf{U}_{h,0}$ and $\phi_h \in V_{h,0}$,

$$(I_h^{st})'(\mathbf{u}_h, z_h; \mathbf{v}_h, \phi_h) = a_h(z_h; \mathbf{u}_h, \mathbf{v}_h) + b_h(\mathbf{u}_h; z_h, \phi_h),$$

with

$$a_h(z_h; \mathbf{u}_h, \mathbf{v}_h) := \int_\Omega (z_h^2 + \eta)\, \partial_{\mathbf{F}} W(\nabla \mathbf{u}_h) : \nabla \mathbf{v}_h \, \mathrm{d}\mathbf{x} + 2C \sum_{E \in \mathcal{E}} h_E^\gamma \int_E (z_h^2 + \eta)\, [\mathbf{u}_h] \cdot [\mathbf{v}_h] \, \mathrm{d}s$$

and

$$b_h(\mathbf{u}_h; z_h, \phi_h) := 2 \int_\Omega \left[W(\nabla \mathbf{u}_h)\, z_h\, \phi_h + \alpha \left(\varepsilon \nabla z_h \cdot \nabla \phi_h + \frac{(z_h - 1)\phi_h}{4\varepsilon} \right) \right] \mathrm{d}\mathbf{x} + 2C \sum_{E \in \mathcal{E}} h_E^\gamma \int_E z_h\, \phi_h\, |[\mathbf{u}_h]|^2 \, \mathrm{d}s.$$

We are led to the following numerical scheme.

Algorithm 2.

- Step 1. Given two tolerances $TOL, TOL' > 0$, a positive integer J and initial data $\mathbf{u}_h^0 \in \mathbf{U}_h$ (in our experiments $J = 250$, $TOL = 10^{-5}$, and $TOL' = 10^{-6}$), set $k = 1$ and find $z_h^0 \in V_h$ such that

$$b_h(\mathbf{u}_h^0; z_h^0, \phi_h) = 0, \quad \forall \phi_h \in V_{h,0}.$$

- Step 2. Given z_h^{k-1} and $\mathbf{u}_h^{k-1}$, set $\mathbf{u}_h^{k,0} = \mathbf{u}_h^{k-1}$, $j = 1$ and $t = 0$. Solve the gradient flow equation (3.5) as follows. Find $\mathbf{w}_h^{j-1} \in \mathbf{U}_{h,0}$ such that

$$(\nabla \mathbf{w}_h^{j-1}, \nabla \mathbf{v}_h) = -a_h(z_h^{k-1}; \mathbf{u}_h^{k,j-1}, \mathbf{v}_h), \quad \forall \mathbf{v}_h \in \mathbf{U}_{h,0}. \tag{3.9}$$

  Choose a proper time step $\Delta t > 0$, set $\mathbf{u}_h^{k,j} = \mathbf{u}_h^{k,j-1} + \Delta t\, \mathbf{w}_h^{j-1}$, $t = t + \Delta t$ and $j = j + 1$. Repeat the above process, until $\|\nabla \mathbf{w}_h\| < TOL'$ or $j \geq J$. Set $\mathbf{u}_h^k = \mathbf{u}_h^{k,j}$.
- Step 3. Given $\mathbf{u}_h^k$, find $z_h^k \in V_h$ satisfying

$$b_h(\mathbf{u}_h^k; z_h^k, \phi_h) = 0, \quad \forall \phi_h \in V_{h,0}. \tag{3.10}$$

- Step 4. If $\|z_h^k - z_h^{k-1}\| < TOL$, stop; otherwise, set $k = k + 1$ and go back to Step 2.

The above fully discrete algorithm enjoys the following energy decay property.

Proposition 3.1. *For each h and $k \geq 1$ there exists $\delta > 0$ such that if $0 < \Delta t < \delta$ and $(\mathbf{u}_h^{k-1}, z_h^{k-1})$ and $(\mathbf{u}_h^k, z_h^k)$ are two consecutive solutions generated by Algorithm 2, then*

$$I_h^{st}(\mathbf{u}_h^k, z_h^k) \leq I_h^{st}(\mathbf{u}_h^{k-1}, z_h^{k-1}). \tag{3.11}$$

Proof. As $I_h^{st}(\mathbf{u}_h^k, \cdot)$ is convex, relation (3.10) leads to

$$I_h^{st}(\mathbf{u}_h^k, z_h^k) \leq I_h^{st}(\mathbf{u}_h^k, z_h^{k-1}).$$

We only need show that $I_h^{st}(\mathbf{u}_h^k, z_h^{k-1}) \leq I_h^{st}(\mathbf{u}_h^{k-1}, z_h^{k-1})$. By Step 2 of Algorithm 2, it suffices to prove that $I_h^{st}(\mathbf{u}_h^{k,j}, z_h^{k-1}) \leq I_h^{st}(\mathbf{u}_h^{k,j-1}, z_h^{k-1})$ for all j. Again by Step 2, using the fundamental theorem of calculus we see that

$$\begin{aligned}
&\frac{I_h^{st}(\mathbf{u}_h^{k,j}, z_h^{k-1}) - I_h^{st}(\mathbf{u}_h^{k,j-1}, z_h^{k-1})}{\Delta t} \\
&= \int_\Omega \left((z_h^{k-1})^2 + \eta\right) \left(\int_{\rho=0}^1 \partial_{\mathbf{F}} W(\nabla \mathbf{u}_h^{k,j-1} + \rho \Delta t \nabla \mathbf{w}_h^{j-1}) : \nabla \mathbf{w}_h^{j-1} \mathrm{d}\rho \right) \mathrm{d}\mathbf{x} \\
&\quad + 2C \sum_{E \in \mathcal{E}} h_E^\gamma \int_E \left((z_h^{k-1})^2 + \eta\right) \left[\frac{\mathbf{u}_h^{k,j} + \mathbf{u}_h^{k,j-1}}{2} \right] \cdot [\mathbf{w}_h^{j-1}] \, \mathrm{d}s.
\end{aligned}$$

Since $\mathbf{u}_h^{k,j-1}$ is piecewise affine, there are only a finite number of values of $\det \nabla \mathbf{u}_h^{k,j-1}(\mathbf{x})$, all of which are assumed to be positive. Therefore, there exists $\delta > 0$ such that the family $\{\nabla \mathbf{u}_h^{k,j-1} + \rho \Delta t \nabla \mathbf{w}_h^{j-1}\}_{\rho \in [0,1]}$ is bounded and has determinants away from zero whenever $0 < \Delta t < \delta$. Moreover, as $j \leq J$, we can choose the same δ valid for all j. Hence, the growth condition (2.3) does not represent an obstacle and we may pass to the limit as $\Delta t \to 0$ (we are assuming W to be C^1 on the space of orientation-preserving matrices), yielding

$$\lim_{\Delta t \to 0^+} \frac{I_h^{st}(\mathbf{u}_h^{k,j}, z_h^{k-1}) - I_h^{st}(\mathbf{u}_h^{k,j-1}, z_h^{k-1})}{\Delta t} = a_h(z_h^{k-1}; \mathbf{u}_h^{k,j-1}, \mathbf{w}_h^{j-1}) = -(\nabla \mathbf{w}_h^{j-1}, \nabla \mathbf{w}_h^{j-1}).$$

If $\mathbf{w}_h^{j-1} = \mathbf{0}$, obviously $I_h^{st}(\mathbf{u}_h^{k,j}, z_h^{k-1}) = I_h^{st}(\mathbf{u}_h^{k,j-1}, z_h^{k-1})$. If $\mathbf{w}_h^{j-1} \neq \mathbf{0}$, by choosing δ small enough, we obtain that $I_h^{st}(\mathbf{u}_h^{k,j}, z_h^{k-1}) < I_h^{st}(\mathbf{u}_h^{k,j-1}, z_h^{k-1})$. As there are only a finite number of j's, the number δ can be chosen uniformly in j. This completes the proof. □

We now describe more details of the algorithm and its implementation.

In actual computations, we normally use $a_h(\bar{z}_h^{k-1}; \mathbf{u}_h^{k,j-1}, \mathbf{v}_h)$ in place of the original term $a_h(z_h^{k-1}; \mathbf{u}_h^{k,j-1}, \mathbf{v}_h)$ in (3.9), where $\bar{z}_h^{k-1}$ is piecewise average of z_h^{k-1}, i.e.,

$$\bar{z}_h^{k-1}|_T = \frac{1}{|T|} \int_T z_h^{k-1} \, \mathrm{d}\mathbf{x}$$

for each $T \in \mathcal{T}_h$. In this way, we only need to store a constant in each element, which saves memory and makes the program faster. However, such a choice might affect the energy decay property shown in Proposition 3.1. All in all, numerical experiments show that this simplification speeds up the algorithm significantly and still finds the right minimizer.

In step 2, the time step Δt can be chosen adaptively, as we explain next, following [29]. For each j, we compute $\mathbf{u}^{k,j}$ using the same value of Δt as in the last iteration. We accept $\mathbf{u}^{k,j}$ if $I_h^{st}(\mathbf{u}_h^{k,j}, z_h^{k-1}) < I_h^{st}(\mathbf{u}_h^{k,j-1}, z_h^{k-1})$ and $\det \nabla \mathbf{u}^{k,j} > 0$. Otherwise, we decrease the time step by a predefined factor $\beta \in (0, 1)$, i.e., we set $\Delta t = \beta \, \Delta t$. This is done iteratively until a $\mathbf{u}^{k,j}$ is accepted. In our numerical experiments, we took $\beta = 0.1$ and the initial value of the time step was $\Delta t = 0.02$. In most time steps, no reductions of the form $\Delta t = \beta \, \Delta t$ were necessary. To prevent the time step from becoming too small, we reset $\Delta t = \Delta t / \beta$ every certain number M of steps. In our computations, we set $M = 100$. With this choice of parameters, we saw in [29] that the energy decays quickly in the beginning of the process. That is why we did not choose a very large J; in fact, we set $J = 250$. Numerical experiments showed that such choices make the algorithm find a minimizer.

In step 3, we need to solve a linear problem with the small parameter ε. Therefore, the system matrix may have a large condition number, which can be solved by a direct method or a preconditioning iterative method (see [52]). In our simulations, we chose the standard preconditioned conjugate gradient method. As an initial guess, in the first step we chose $z = 1$ everywhere except on $\partial_N \Omega$ where we put $z = 0$; in step k we chose as an initial guess the solution given by step $k - 1$.

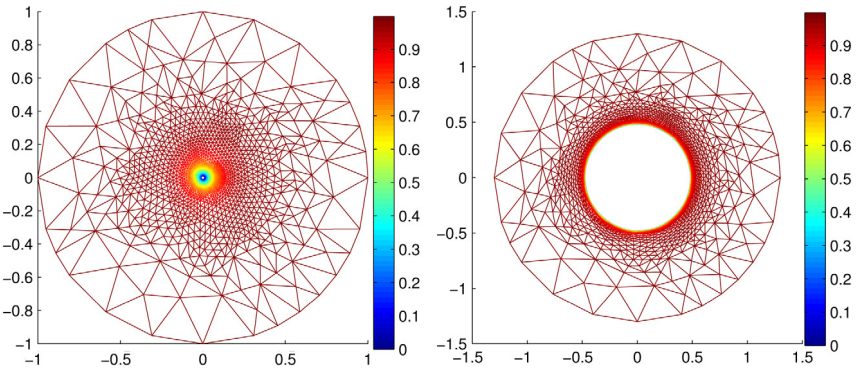

Fig. 4.1. A ball with one micro-hole at the centre, $\lambda = 1.3$.

4. Void coalescence and fracture in domains with micro-holes

In all experiments of the paper (except those of Section 8), we take the stored energy function as in [29]:

$$W(\mathbf{F}) = \frac{|\mathbf{F}|^p}{p} + (\det \mathbf{F} - 1)^2 + \frac{2^{p/2-1}}{\det \mathbf{F}} - c_0, \tag{4.1}$$

with $c_0 = 2^{p/2}/p + 2^{p/2}/2$. Recall that $|\mathbf{F}|$ is the Frobenius norm of $\mathbf{F}$. In Sections 4–7 we take $p = 1.5$; in Section 8 we study the effect of choosing a larger exponent p (and a slightly different form of W). In this section we consider a domain Ω with micro-holes, as in (2.4).

4.1. A ball with one micro-hole

We initially test the case when there is only one micro-hole in the material. These experiments are to be compared with those in [29] where fracture was not allowed. The domain Ω is $B(\mathbf{0}, 1)$, whereas Ω_δ is $\Omega \setminus B(\mathbf{a}, \delta)$ with $\delta = 0.01$. The boundary condition prescribes $\mathbf{u}(\mathbf{x}) = \lambda \mathbf{x}$ on $\partial B(\mathbf{0}, 1)$. We set $\eta = 10^{-7}$, $\alpha = 1$ and $\varepsilon = 0.01$ (see (2.7)). We do experiments for various $\mathbf{a}$ and λ. The initial condition is given by $\mathbf{u}_0(\mathbf{x}) = \lambda \mathbf{x}$.

All the figures in this section have the same structure: the left and right parts represent, respectively, the reference and deformed configurations; the colourmap in both subfigures shows the value of the damage function z_h.

Firstly, we set $\mathbf{a} = (0, 0)$. When $\lambda = 1.3$, radial cavitation occurs, as shown in Fig. 4.1. We do not speak of fracture since the blue part of z_h in the reference configuration has a tiny two-dimensional measure. Fig. 4.1 is, in fact, quite similar to those obtained in [29]; this is natural since, in the absence of fracture, both models coincide. As λ becomes larger, fracture appears near the cavity. When $\lambda = 1.4$, we observe a crack in the form of a short, almost straight curve that passes through the cavity and dies away in two crack tips. Fig. 4.2 shows the result for $\lambda = 1.7$, where a crack appears with three longer arms that radiate from the micro-hole. The asymmetry of the crack path might be due to mesh inhomogeneity.

When the micro-hole moves away from the origin, the shape of the fracture changes; this effect of the micro-hole location also appears in the pure cavitation problem (see [29]). In Fig. 4.3 we show the outcome for $\mathbf{a} = (0.6, 0)$ and $\lambda = 1.7$: we can see that there are only two crack paths stretching away from the boundary.

4.2. A ball with two micro-holes

We consider $\Omega = B(\mathbf{0}, 1)$, Ω_δ as in (2.4) with $\mathbf{a}_1 = (0, 0)$, $\mathbf{a}_2 = (0, 0.5)$ and $\delta = 0.01$. We set the boundary condition of $\mathbf{u}(\mathbf{x}) = \lambda \mathbf{x}$ on the Dirichlet boundary $\partial\Omega$ for some $\lambda > 1$. The Neumann boundary is $\partial B(\mathbf{a}_1, \delta) \cup \partial B(\mathbf{a}_2, \delta)$. The initial deformation is taken to be $\mathbf{u}_0(\mathbf{x}) = \lambda \mathbf{x}$. We choose $\eta = 10^{-7}$, $\varepsilon = 0.005$ and $\alpha = 1$. We run our algorithm for various λ from 1.3 to 1.6.

Fig. 4.4 illustrates the numerical results for $\lambda = 1.3$. We can see that the two small holes expanded to two larger holes after the deformation, so cavitation occurs. We also see that there is no serious material damage in this case

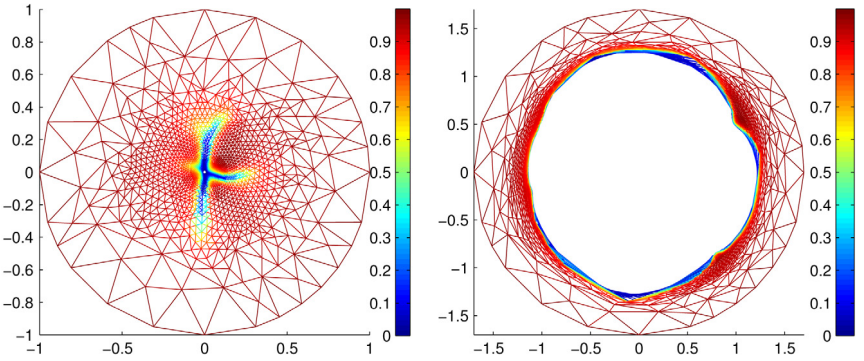

Fig. 4.2. A ball with one micro-hole at the centre, $\lambda = 1.7$.

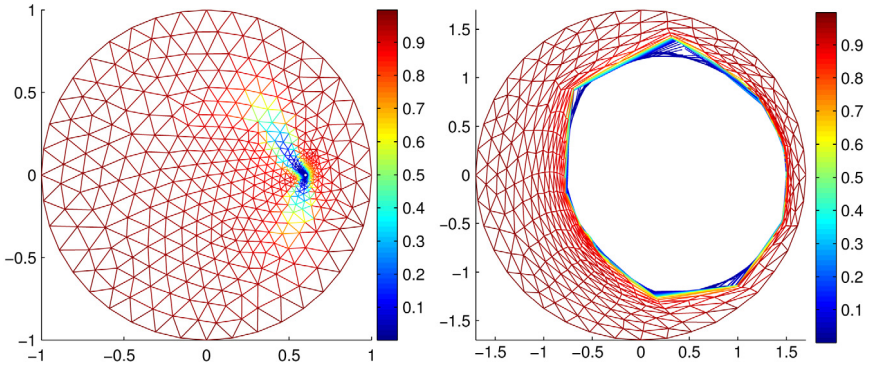

Fig. 4.3. A ball with one micro-hole at $\mathbf{a} = (0.6, 0)$, $\lambda = 1.7$.

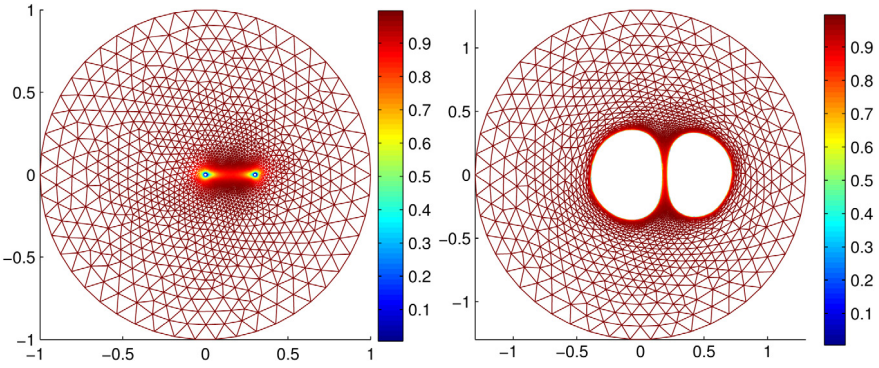

Fig. 4.4. A ball with two micro-holes, $\lambda = 1.3$.

(that is, fracture does not appear), because the blue part of z_h is concentrated around the two holes in the reference configuration, and is hardly visible in the deformed configuration.

Fig. 4.5 shows the numerical results for $\lambda = 1.5$. From the left subfigure, we can see that the material is fully damaged in the region between the two small holes: the fracture path goes through the region and connects the two holes. From the right subfigure, we can see that two holes merge into a larger hole, ignoring the damaged thin strip in the middle, where $z_h \simeq 0$. We interpret this as void coalescence.

4.3. A slab with three micro-holes

In this example, we consider a slab with three holes, so that $\Omega_\delta = (-0.5, 0.5) \times (0, 0.4) \setminus (\bigcup_{i=0}^{2} B(\mathbf{a}_i, \delta))$. We take $\delta = 0.01$ and $\mathbf{a}_0 = (0, 0.1)$, $\mathbf{a}_1 = (0, 0.2)$, $\mathbf{a}_2 = (0, 0.3)$. The lateral sides of the slab form the Dirichlet boundary,

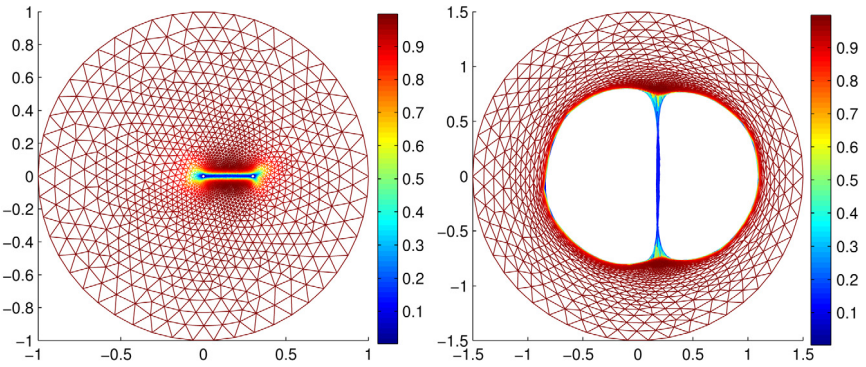

Fig. 4.5. A ball with two micro-holes, $\lambda = 1.5$.

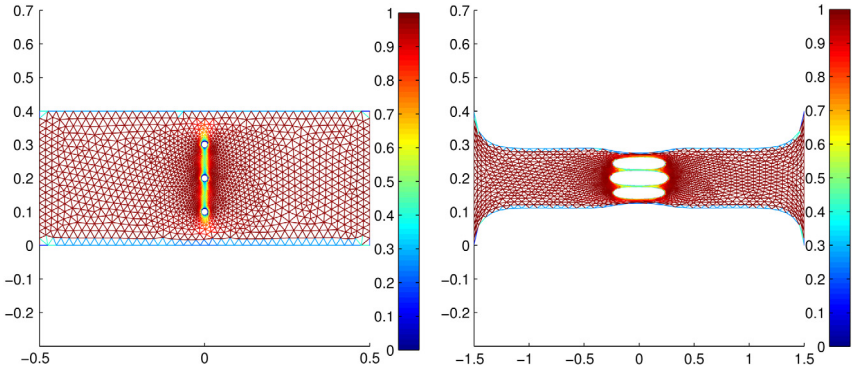

Fig. 4.6. A slab with three micro-holes, $\lambda = 3$.

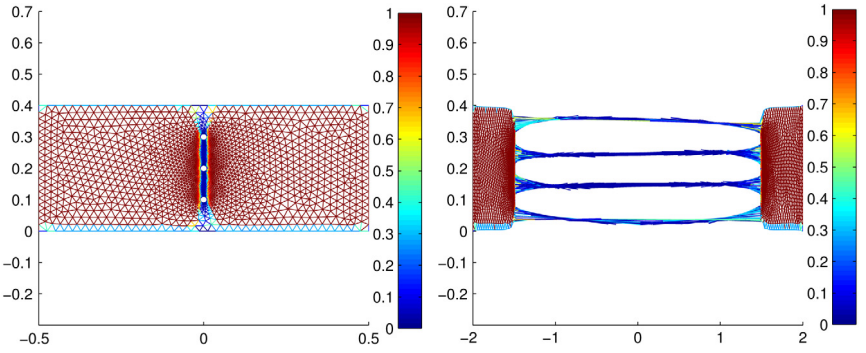

Fig. 4.7. A slab with three micro-holes, $\lambda = 4$.

where we impose the condition $\mathbf{u}_D(\mathbf{x}) = (\lambda x_1, x_2)$. The upper and lower sides, together with the boundary of the micro-holes, form the Neumann boundary. The initial deformation is $\mathbf{u}_0(\mathbf{x}) = (\lambda x_1, x_2)$. We set $\eta = 10^{-7}$, $\varepsilon = 0.002$ and $\alpha = 0.5$.

We did experiments for various λ. When $\lambda = 3$ (see Fig. 4.6), the material is not fractured, although the holes increased largely. For $\lambda = 4$ (see Fig. 4.7), the material is broken apart into two pieces by a crack that, in the reference configuration, is nearly a vertical line passing through the micro-holes.

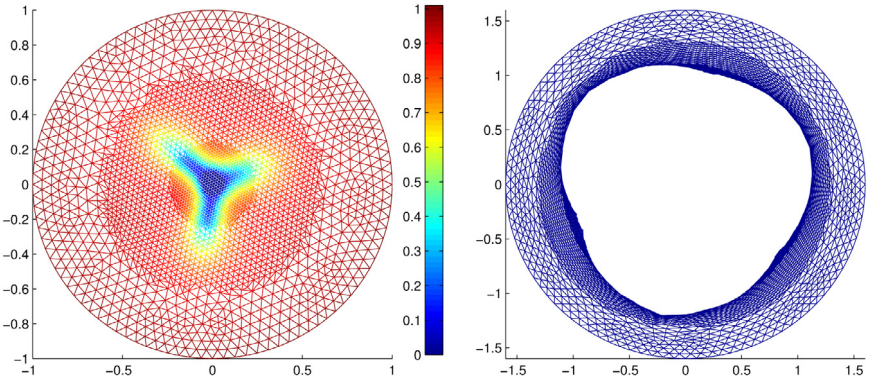

Fig. 5.1. A perfect ball, $\lambda = 1.6$.

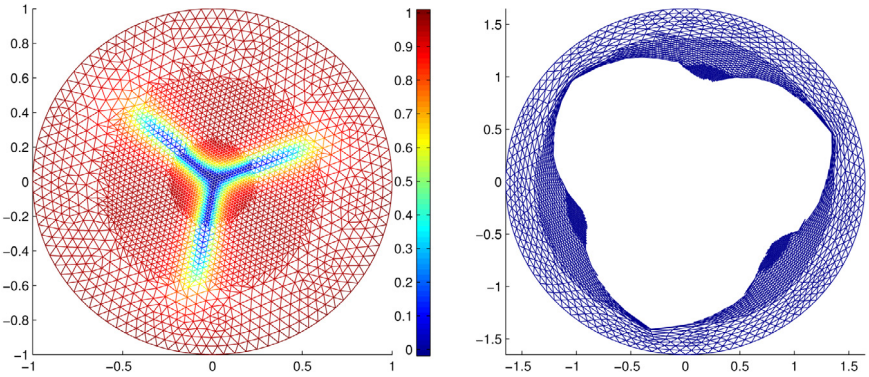

Fig. 5.2. A perfect ball, $\lambda = 1.65$.

5. Failure in a perfect ball

In this section we show the experiments for a ball without micro-holes so as to visualize the cavity or crack nucleation. Let the computational domain be $\Omega = B(\mathbf{0}, 1)$. The boundary condition is $\mathbf{u}_D(\mathbf{x}) = \lambda\mathbf{x}$ on $\partial\Omega$. We set $\eta = 10^{-7}$, $\alpha = 1$ and $\varepsilon = 0.025$. We set the homogeneous deformation $\mathbf{u}_0 = \lambda\mathbf{x}$ as the initial deformation.

We run the program for various λ from 1.3 to 1.8. We found that there is a critical point λ_0 between 1.575 and 1.6. When $\lambda < \lambda_0$, the resulting deformation is still homogeneous and the material is healthy. For example, when $\lambda = 1.5$, the value of z_h is about 0.82 in the central area. Hence the material is healthy, and the relatively large deviation of z_h from 1 is due to the relatively large value of ε.

When $\lambda > \lambda_0$, the resulting deformations, far from being homogeneous, exhibit fracture. After running the experiments on a uniform mesh, we found a significant improvement in the accuracy when the mesh was refined around the centre. The figures in this section are therefore done for a refined mesh. In the rest of the paper, in the right subfigures, we illustrate only the deformation in the healthy part of the body and omit the deformation in the damaged material (when $z_h < 0.3$); the colour has been arbitrarily chosen to be blue. The deformation for $\lambda = 1.6$ is shown in Fig. 5.1, where we can see a fracture with a triple junction, in which the three arms meet at $2\pi/3$ degrees (see [64] for the relevance of triple junctions in the Mumford–Shah functional).

This kind of fracture grows with increasing λ. For example, Fig. 5.2 shows the situation for $\lambda = 1.65$, where we used as an initial value a scaled version of the deformation in Fig. 5.1. We can see a perfect triple junction in the reference configuration.

Our experiments show that when λ is near the critical value, the final solution depends on the initial condition. A typical case is $\lambda = 1.575$: when we use the homogeneous deformation as the initial function, we get a uniform deformation. In contrast, if we use a fractured deformation (like a scaled version of the final solution found for $\lambda = 1.6$ in Fig. 5.1) we get a fractured deformation. The reason for this initial-value dependence is the presence of several local minimizers and energy barriers between them. Instead, when we run the same experiments for $\lambda = 1.55$

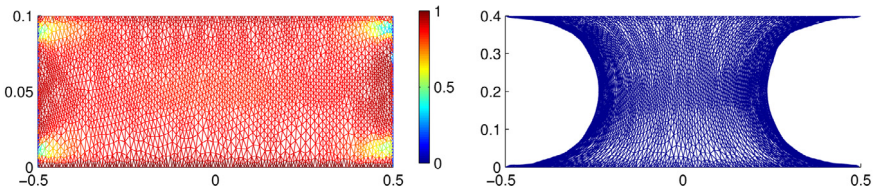

Fig. 6.1. A bar: $(-0.5, 0.5) \times (0, 0.1)$, $\lambda = 4$.

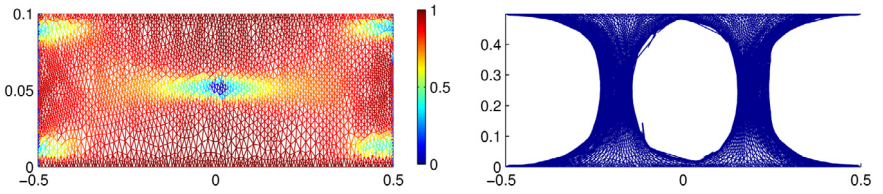

Fig. 6.2. A bar: $(-0.5, 0.5) \times (0, 0.1)$, $\lambda = 5$.

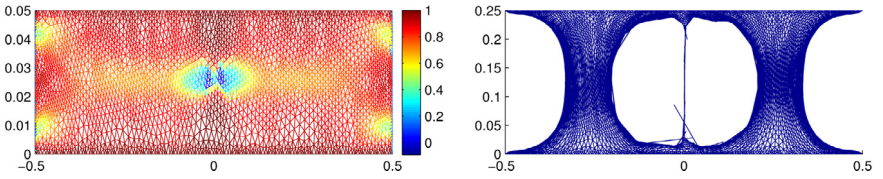

Fig. 6.3. A thinner bar: $(-0.5, 0.5) \times (0, 0.05)$, $\lambda = 5$.

and 1.5, both initial values lead to a homogeneous non-fractured deformation. This is in contrast with the numerical experiments for the pure cavitation problem with micro-holes [29], where the computed deformation does not depend on the initial values. The existence of multiple local minimizers indicates that, for the material failure simulations, it is more realistic to study the quasistatic evolution process with an increasing stress λ.

6. Gent and Lindley's experiments

In this section, we show how our model can simulate the celebrated experiments by Gent and Lindley [1]. We first consider the thin two-dimensional bar $\Omega = (-0.5, 0.5) \times (0, 0.1)$. We set the Dirichlet condition $\mathbf{u}(x_1, x_2) = (x_1, \lambda x_2)$ on the top and bottom edges of Ω. The Neumann part consists of the lateral sides. We set $\eta = 10^{-7}$, $\varepsilon = 0.001$ and $\alpha = 0.2$. The initial value is chosen as $\mathbf{u}_0(x_1, x_2) = (x_1, \lambda x_2)$.

We run the experiments for various λ from 3 to 5. We found the existence of a critical point λ_0 between 4 and 5. When $\lambda < \lambda_0$, as shown in Fig. 6.1, the material is still healthy. When $\lambda > \lambda_0$, as shown in Fig. 6.2, a big cavity appears at the centre of the bar, where $z_h \simeq 0$ (the material is damaged there).

We also tested the two thinner bars $(-0.5, 0.5) \times (0, 0.05)$ and $(-0.5, 0.5) \times (0, 0.025)$. All other conditions are similar to the previous studies. When the height of the bar is 0.05 (Fig. 6.3), we can observe two cavities in the centre. When the height is further reduced to 0.025 (Fig. 6.4), we observe seven cavities in the middle of the bar. This is consistent with the experimental observations by Gent and Lindley [1], where they observed that the number of created cavities substantially increases as the test-piece becomes thinner (the reason being that a smaller free surface has a more limited ability to release the hydrostatic tension produced by the kinematic constraint of incompressibility).

We also note that in Figs. 6.1–6.4 the region in which v is far from 1 and 0 (in particular, the yellow region, where $v \simeq 0.6$) is still too large. This is due to the relative large value of ε (in comparison with the height of the domain) chosen in the experiments. A further study of this case would need to reduce the value of ε and, simultaneously, use an adaptive method to refine the meshes, as well as some accelerating numerical techniques.

7. Materials with rigid inclusions

We illustrate some numerical experiments for materials with rigid inclusions. We consider the square domain $\Omega = (-0.2, 0.2) \times (0, 0.4)$.

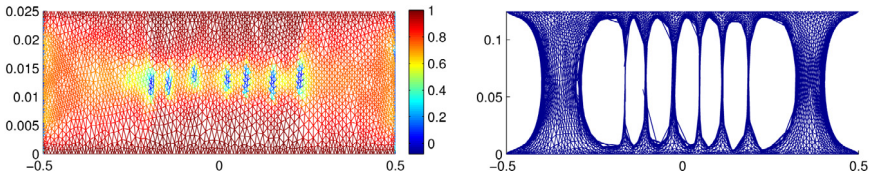

Fig. 6.4. An even thinner bar: $(-0.5, 0.5) \times (0, 0.025)$, $\lambda = 5$.

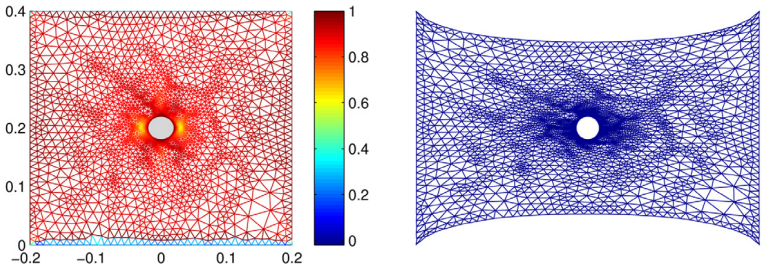

Fig. 7.1. A square with a rigid inclusion, $\lambda = 1.475$.

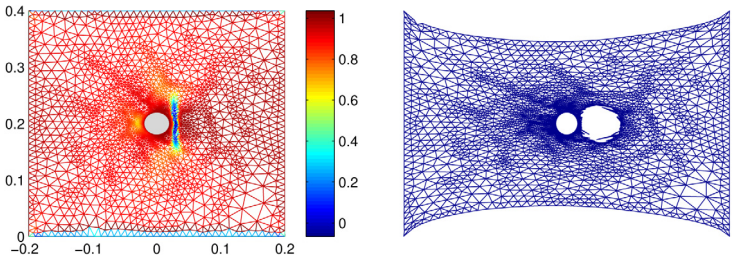

Fig. 7.2. A square with a rigid inclusion, $\lambda = 1.48$.

7.1. One rigid inclusion

We put a small circular hard core $B((0, 0.2), R)$, with radius $R = 0.02$, in the centre of Ω. On $\partial B((0, 0.2), R)$ we set $\mathbf{u}(\mathbf{x}) = \mathbf{x}$ and $z(\mathbf{x}) = 1$ (the elastic material is fixed on the surface of the inclusion). We set the Dirichlet boundary condition $\mathbf{u}(\mathbf{x}) = (\lambda x_1, x_2)$ and $z(\mathbf{x}) = 1$ on the lateral sides of the square $\partial\Omega$. The Neumann part consists of the top and bottom edges of Ω. We set $\eta = 10^{-7}$, $\varepsilon = 0.001$ and $\alpha = 0.01$. For the initial value, we choose $\mathbf{u}_0(x_1, x_2) = (f(x_1), x_2)$, with

$$f(x_1) = \begin{cases} x_1 & \text{if } |x_1| \le R, \\ \dfrac{\lambda(|x_1| - R) + (0.2 - |x_1|)}{0.2 - R} x_1 & \text{if } |x_1| \ge R. \end{cases}$$

We did experiments for several values of λ. As in the previous sections, there is a critical λ_0 between 1.475 and 1.48. When $\lambda < \lambda_0$, the material is healthy. When $\lambda > \lambda_0$, the body breaks at a well-defined location near the pole of the inclusion; this is consistent with the experiments in, e.g., [7,72,73]. The fact that a cavity opens first at the *right* of the pole is probably due to the mesh inhomogeneity. As λ increases, a second cavity opens (this time at the left of the inclusion). In the reference configuration we see two vertical cracks (one on each side) which grow until they merge and tear the specimen completely apart. Figs. 7.1–7.4 show this process.

7.2. Two rigid inclusions

We illustrate some numerical tests for materials with two rigid inclusions. The reference domain is the square Ω with the two circular cores $B((-0.035, 0.2), R)$ and $B((0.035, 0.2), R)$ of radius $R = 0.02$. We suppose that the elastic material is glued to the surface of the inclusions. The locations of the two hard cores after the deformation

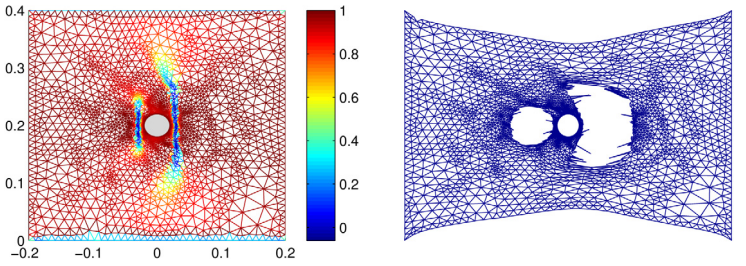

Fig. 7.3. A square with a rigid inclusion, $\lambda = 1.485$.

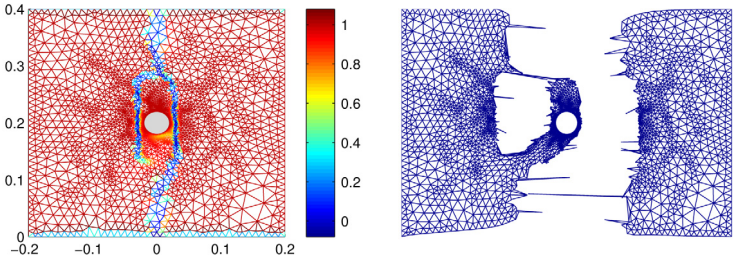

Fig. 7.4. A square with a rigid inclusion, $\lambda = 1.5$.

are not prescribed, so they need to be computed: this introduces extra difficulties in the numerical simulations. In this paper, we do not discuss general methods to deal with such difficulties but, instead, we use a simple technique to search for the optimal locations of the hard cores. Exploiting the symmetry of the problem, we assume that the two cores can only move horizontally in opposite directions. In each iteration of Algorithm 2 (see Section 3.3), we consider three different scenarios for the location of the two cores: (a) they become closer than in the previous step by a small distance δ (taken to be 0.0001λ in our experiments); (b) they do not change their positions; (c) they move apart by the same distance δ. Once the locations of the hard cores are fixed for each case, the Dirichlet boundary condition for $\mathbf{u}$ is known. Hence, we can compute $\mathbf{u}$ and z by Step 2 and Step 3, respectively, in each of the three cases. Then, we compare the total energy for them and choose, as the final result in the iteration, the resulting $\mathbf{u}_h$ and z_h corresponding to the smallest energy. Those $\mathbf{u}_h$ and z_h act as the initial conditions for the next iteration.

On the first step, we set the continuous initial deformation $\mathbf{u}_0(x_1, x_2) = (\tilde{f}(x_1), x_2)$ as the initial value, with

$$\tilde{f}(x_1) := \begin{cases} (0.035\lambda - R)\dfrac{x_1}{0.035 - R} & \text{if } |x_1| \le 0.035 - R, \\ 0.035\,\mathrm{sgn}(x_1)(\lambda - 1) + x_1 & \text{if } |x_1 \pm 0.035| \le R, \\ \dfrac{\lambda(|x_1| - R - 0.035) + \sigma(0.2 - |x_1|)}{0.2 - R - 0.035} x_1 & \text{if } |x_1| \ge R + 0.035 \end{cases}$$

and $\sigma := (0.035\lambda + R)/(0.035 + R)$. The function $\mathbf{u}_0$ satisfies the stretching Dirichlet boundary condition $\mathbf{u}(\mathbf{x}) = (\lambda x_1, x_2)$ on the lateral sides of the square, and also changes the position of the two cores. All other settings are the same as in the simulations with only one inclusion. We carried out experiments for different values of λ from 1.3 to 1.5. We observed a critical value for λ between 1.4 and 1.41. When λ is less than the critical value (see Fig. 7.5 for $\lambda = 1.4$), the material is still healthy, although there is a yellow region for z between the two hard cores, which indicates that material failure will initiate there. When λ is larger than the critical value (see Fig. 7.6 for $\lambda = 1.41$), the body is completely cut by a crack that runs perpendicular to the direction of the tensile load. The observations are consistent with the experimental results of [7,2].

8. Growth of the stored-energy density at infinity

One of the main properties that the stored-energy function is assumed to possess in the existence theory for nonlinear elasticity [61,74,75] is that $W(\mathbf{F}) \to \infty$ sufficiently fast as the deformation gradient $\mathbf{F}$ grows unbounded. For stored energies of the form (2.2), the exponent p in $\frac{\mu}{p}|\mathbf{F}|^p$ is imposed to be larger than or equal to the space

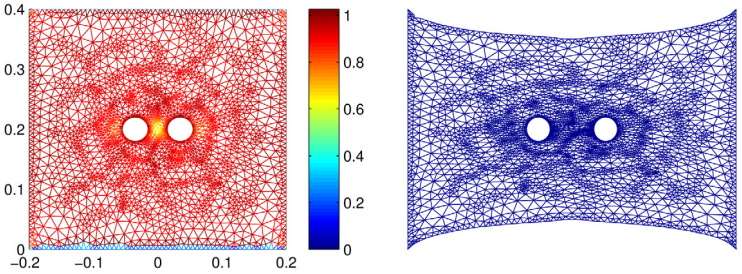

Fig. 7.5. A square with two rigid inclusions, $\lambda = 1.4$.

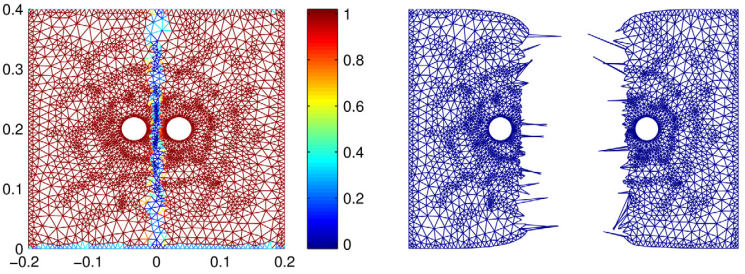

Fig. 7.6. A square with two rigid inclusions, $\lambda = 1.41$.

dimension n. As mentioned before (2.3), this condition is precisely the opposite of what is required for cavitation, in the sense that

- If $p > n$, then, by the Sobolev embedding theorem [76–78], any map $\mathbf{u} \in W^{1,p}(\Omega)$ is necessarily continuous and cannot develop cavitation singularities (a cavity cannot originate at a single point). When $p = n$, not all maps in $W^{1,p}(\Omega)$ are continuous, yet they must be such that $\operatorname{Det} \nabla \mathbf{u} = \det \nabla \mathbf{u}$, which for invertible maps means that $\mathbf{u}$ creates no cavities [61,18].
- In the case of a domain Ω_δ with pre-existing micro-holes of radius δ, as in (2.4), if $p < n$, then for every fixed but sufficiently large multiaxial tensile load, the total volume of the holes, computed in the deformed configuration, converges to a positive value as $\delta \to 0$; when $p \geq n$, the holes tend to close (their total volume tends to zero) as $\delta \to 0$ (see [11,12] and the references therein). Another way of thinking of it is that the load required to increase the total cavity volume by a given factor (or the total energy required for cavitation) tends to infinity as $\delta \to 0$; some quantitative estimates are given in [79].

In spite of the previous analytical results, in order to model cavitation it is probably better to consider the situation of a body containing a number of defects (which may either come from the manufacturing process or result from the breaking of atomic bonds or polymer chains) whose initial size δ is small but does not really tend to zero. In the regularized model for fracture that we study in this paper, ε plays the role of this δ since cavitation is modelled by the appearance of balls of radius ε where the material is damaged and stretches as much as necessary in order to accommodate to the deformation of the rest of the body. Since ε is a fixed positive number (it does not tend to zero in the simulation, even if it is small), it will always be possible to numerically observe cavitation, even if $p \geq n$ (although the load at which this occurs becomes larger for smaller values of ε). On the other hand, a larger value of p corresponds to a body that cannot sustain large deformations and prefers to develop brittle fracture (jump discontinuities across surfaces) rather than stretching the wall of a small cavity in a substantial manner.

From the previous arguments it may be concluded that whether to choose an exponent $p < n$ or $p \geq n$ in a stored-energy function of the form (2.2) (or an exponent $q \geq \frac{n}{n-1}$ in a stored-energy function of the form $W(\mathbf{F}) = \alpha|\mathbf{F}|^p + \beta|\operatorname{cof}\mathbf{F}|^q + f(\det \mathbf{F})$ in dimension $n = 3$) is an important part of the definition of the model and should be expected to affect the mechanical behaviour of the material during the initiation of fracture. Here we contribute to this discussion by changing the exponent $p = 1.5$ to $p = 2$ and $p = 3$ in the experiments of Figs. 5.1,

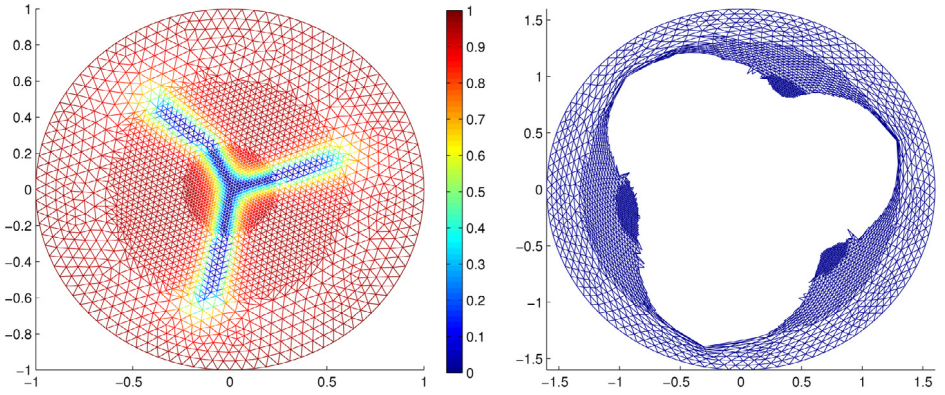

Fig. 8.1. Fracture of a perfect ball, $\lambda = 1.6$, $\varepsilon = 0.025$, $p = 2$.

6.4 and 7.3. To be more precise, and to perform a fair comparison, instead of (4.1) we use the energy

$$W(\mathbf{F}) = a\left(\frac{|\mathbf{F}|^p}{p} + \frac{2^{p/2-1}}{\det \mathbf{F}}\right) + \frac{b}{2}(\det \mathbf{F} - 1)^2 - c_0, \tag{8.1}$$

where c_0 is as before, and $a, b > 0$ are suitable constants to be determined below. Note that the choice $a = 1$ and $b = 2$ gives rise to the energy (4.1). A straightforward calculation shows that the Piola–Kirchhoff stress tensor $\mathbf{T}_R = \partial_{\mathbf{F}} W$ satisfies $\mathbf{T}_R(\mathbf{I}) = \mathbf{0}$, where $\mathbf{I}$ is the identity matrix, and the stiffness (or *linear elasticity*) tensor $\mathbf{C} = \partial^2_{\mathbf{F}} W(\mathbf{I})$ has the expression

$$\mathbf{C} : \mathbf{H} = 2\mu \frac{\mathbf{H} + \mathbf{H}^T}{2} + \lambda\,(\operatorname{tr} \mathbf{H})\,\mathbf{I} \quad \text{with} \quad \mu = 2^{p/2-1}\,a \text{ and } \lambda = \mu\,\frac{p}{2} + b,$$

for any matrix $\mathbf{H}$. In other words, λ and μ are the Lamé parameters of the material. If now we choose, for a given p, the coefficients

$$a = a(p) = 2^{-\frac{2p-3}{4}} \quad \text{and} \quad b = b(p) = 2 - \frac{2p-3}{4 \cdot 2^{1/4}}, \tag{8.2}$$

we obtain that the corresponding Lamé parameters become

$$\mu = 2^{-1/4} \quad \text{and} \quad \lambda = 2^{-1/4}\,\frac{3}{4} + 2,$$

which do not depend on p. In particular, for $p = 1.5$ we obtain that the values (8.2) are $a = 1$, $b = 2$, so we recover the energy of Sections 4–7.

In the present section we will perform the experiments for $p = 2$ and $p = 3$ with the corresponding a and b of (8.2). The comparison is fair since all give rise to materials with the same Lamé parameters, while their difference relies on the behaviour for large strains. For convenience, we present in the next table the values of a, b.

p	a	b
1.5	1	2
2	$2^{-1/4} = 0.840896$	$2 - 2^{-9/4} = 1.789776$
3	$2^{-3/4} = 0.594604$	$2 - 3 \cdot 2^{-9/4} = 1.369328$

The numerical results are shown in Figs. 8.1–8.5.

In the case of a perfect ball (Figs. 8.1 and 8.2), we observe that the area of the damaged region increases with p and that the shape of the cracks is affected. Fracture is also observed earlier in materials with a larger p: the critical nucleation load decreases from $\lambda \approx 1.58$ when $p = 1.5$ to $\lambda \approx 1.56$ when $p = 3$; this agrees with the interpretation that if the body cannot sustain large deformations, then it is more rigid and, hence, more brittle.

The fact that the critical load decreases with p is also observed in the cases of a thin bar and of a material with a hard inclusion. For the thin bar with height 0.025, we took $p = 3$ and found that the critical load decreases to

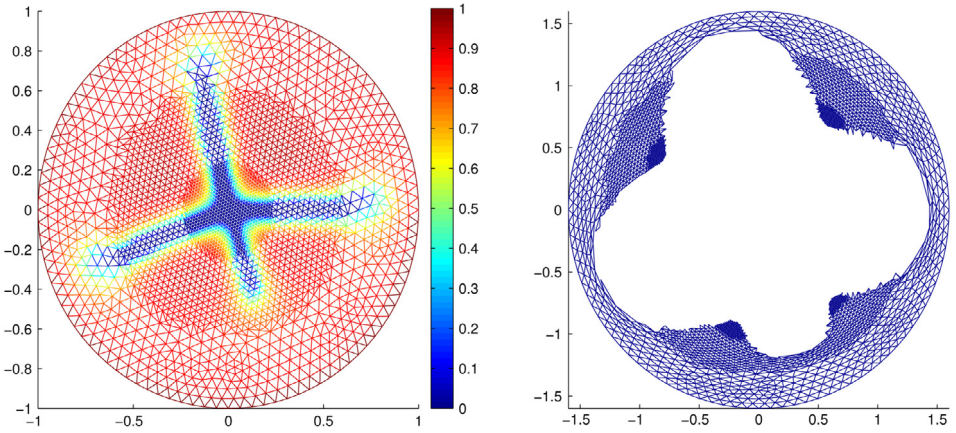

Fig. 8.2. Fracture of a perfect ball, $\lambda = 1.6$, $\varepsilon = 0.025$, $p = 3$.

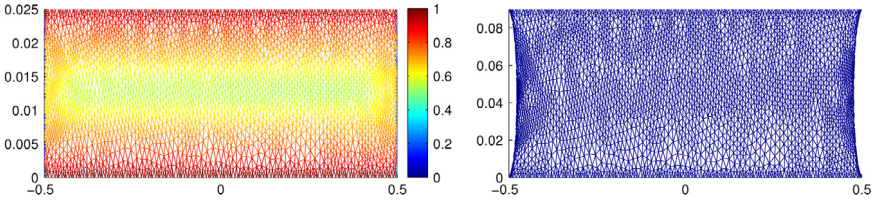

Fig. 8.3. Uniaxial tension of a thin bar, $\Omega = (-0.5, 0.5) \times (0, 0.025)$, $\lambda = 3.6$, $p = 3$.

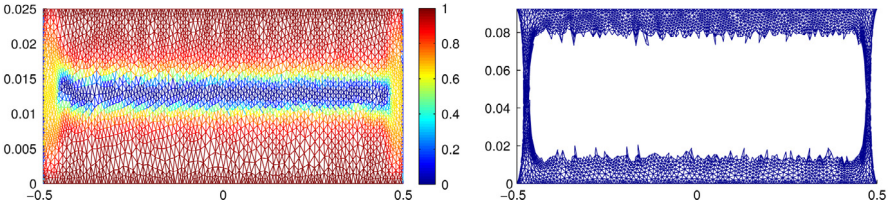

Fig. 8.4. Uniaxial tension of a thin bar, $\Omega = (-0.5, 0.5) \times (0, 0.025)$, $\lambda = 3.7$, $p = 3$.

$\lambda \approx 3.65$: this is shown in Figs. 8.3–8.4. The deformation of Fig. 8.3 (done for $\lambda = 3.6$) presents no fracture, but the wide yellow region that crosses the sample longitudinally by its centre indicates that fracture will appear there. This is confirmed in Fig. 8.4 (done for $\lambda = 3.7$), where the body is divided into two pieces by a large single crack. A comparison of Figs. 8.3–8.4 with Fig. 6.4 (done for $\lambda = 5$ and $p = 1.5$) shows that cavitation is not favourable as a failure mechanism when $p = 3$ (in fact, when $p \geq 2$ in dimension 2).

For the square material with a hard core, the critical load decreases from $\lambda \approx 1.48$ when $p = 1.5$ to $\lambda \approx 1.41$ when $p = 3$. Moreover, when $p = 3$ the material immediately breaks apart into two pieces at the critical load (Fig. 8.5; there are no intermediate situations), whereas in the case $p = 1.5$ we needed a load of $\lambda = 1.5$ (Fig. 7.4) to obtain a similar crack. We also did experiments for $p = 2$ and found similar situations to those for $p = 3$.

The above discussion shows that the restriction $p < n$ is essential to model rubber-like materials in which cavitation occurs, whereas $p \geq n$ models brittle materials.

9. Conclusions

We performed numerical experiments for a phase-field model for fracture in 2D nonlinear elasticity. The model is able to describe both cavitation and fracture. The algorithm relies on alternating minimization, an H^1-gradient flow and a stabilized Crouzeix–Raviart finite element. Our simulations show that:

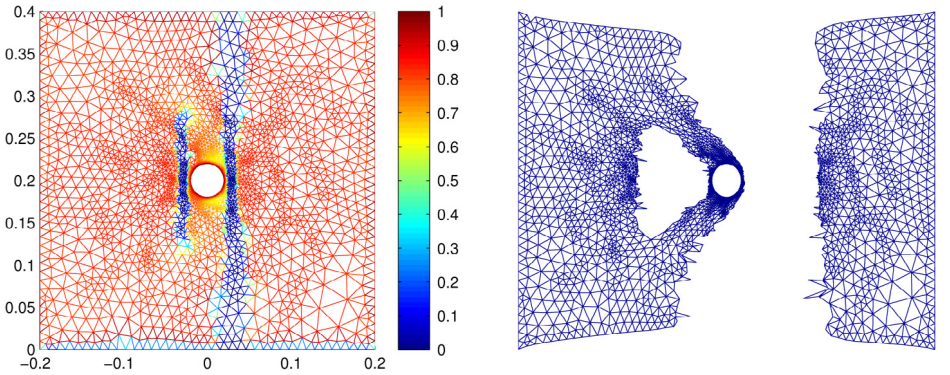

Fig. 8.5. Uniaxial tension of a square with a rigid inclusion, $\lambda = 1.42$, $\varepsilon = 0.001$, $p = 3$.

1. In domains with one micro-hole, a rapid expansion (cavitation) of the hole is produced, followed by fracture near the surface of the hole. When there are multiple micro-holes, rapid expansions of the holes are produced, followed by a crack connecting the holes, which provides an explanation for void coalescence.
2. Our model is able to predict the nucleation of cavities and cracks in perfect materials (without pre-existing micro-holes).
3. We simulated the experiments of Gent and Lindley [1], where a thin bar is pulled over its top and bottom. We found that the body prefers to break at a number of small regions rather than creating a truly codimension-one crack (that is, cavitation is preferred over brittle fracture as a mechanism of internal rupture, even at the price of having to sustain the large deformations at the cavity walls). The number of cavities created increases as the domain becomes thinner, in agreement with the experiments of Gent and Lindley.
4. In an elastic body with a rigid inclusion subject to uniaxial tension, the stress concentrates near the inclusion and eventually causes the body to rupture. In the presence of two rigid inclusions, fracture is nucleated between the two inclusions.
5. The restriction $p < n$ (where p is as in (2.2)) is important to model rubber-like materials in which cavitation occurs, whereas $p \geq n$ models brittle materials.

Special mention ought to be made of the recent work by Lefèvre, Ravi-Chandar and Lopez-Pamies [39]. Using four-node hybrid linear elements with constant pressure in a commercial finite element package, they compute the stresses in the interior of short cylinders of various aspect ratios, made of an incompressible neo-Hookean material, subjected to increasing displacement loads from above and below. Guided by the approximate criterion for the onset of cavitation of Lopez-Pamies, Idiart and Nakamura [37], they conclude that the formation and sudden growth of cavities will be observed first along the centre-line of the test-piece, but at the top and bottom surfaces (corresponding to the rubber/plates interfaces in Gent and Lindley's experiments) and not at the centre of the cylinder. With this information in hand they introduce a series of periodically distributed initial micro-holes in the domain, located at three different heights: on the top and bottom surfaces and in the middle plane. They confirm that indeed it is the cavities on the surfaces which grow first; however, they soon stop growing due to the rigidity imposed by the displacement on the boundary. When this occurs, the cylinders relieve their internal stresses by triggering the rapid enlargement of the micro-holes at the middle plane. Once these attain a certain size, the body prefers to activate the cavities that are farther away from the centre-line (those closer to the lateral surfaces) rather than to continue stretching the already enlarged surfaces. The authors complement their remarkable study of the cascading sequence of cavitation events in Gent and Lindley's experiment with a simulation of the tensile loading of an incompressible neo-Hookean bar containing two rigid inclusions. They specifically introduce micro-holes at the poles and at the midpoint between the inclusions, observing the growth of an elongated cavity in the direction of the applied load.

In spite of the insight gained by their study, it still needs to be completed, mainly in two directions. On the one hand, there is some disagreement in the stress–strain relationships that they obtain and those reported in the experimental studies. As the authors mention, this disagreement is due, in part, to the fact that as the cavities grow there must be fracture on the cavity walls, affecting the mechanical behaviour of the whole specimen (for instance, the cavity in the experiment with two rigid inclusions should not elongate in the direction of the load, but turn into a crack that is perpendicular to that direction). This is especially true if the created cavities coalesce. On the other hand, the authors

have to place a large number of micro-cavities by hand, deciding carefully their locations a priori and very finely discretizing the domain around them. The regularized free-discontinuity model for cavitation and fracture presented in [50] and in this paper will serve to complete their analysis since it accounts for the nucleation of cracks during the rapid enlargement of a small cavity; it predicts the coalescence of voids; and it detects automatically the optimal location for fracture without having to add micro-holes to the computational domain beforehand. The differences between the two approaches, and the way they can complement each other, can be seen in the numerical examples of Sections 6 and 7.

Future work includes the development of adaptive methods and of a faster optimization scheme, as well as a study of the limit behaviour of the energy minimizers as $\varepsilon \to 0$ and in the incompressible limit (obtained, for example, by replacing the term $(\det \mathbf{F} - 1)^2$ in (4.1) with $\sigma(\det \mathbf{F} - 1)^2$ and letting $\sigma \to \infty$). This would allow for a more detailed and quantitative comparison between the predictions of our model, the recent work of Lefèvre, Ravi-Chandar and Lopez-Pamies [39], the numerical study of Stringfellow and Abeyaratne [73], and the experimental studies by Gent and Lindley [1], Oberth and Bruenner [72], Gent and Park [7] and Bayraktar, Bessri and Bathias [5], among others. It would be important to analyse possible dependences of the shapes and the propagation of the nucleated fractures on the mesh. Faster techniques are also needed to minimize the functional with surface tension (which takes into account the area of the created surfaces computed in the deformed configuration, as explained in Section 2.3); a more careful study of the effect of adding this energy is also pending.

Acknowledgements

Inspiring discussions with S. Burke, O. Lopez-Pamies and C. Ortner are gratefully acknowledged. D.H. has been supported by FONDECYT projects 11110011 and 1150038 of the Chilean Ministry of Education and by the Millennium Nucleus Center for Analysis of PDE NC130017 of the Chilean Ministry of Economy. C.M.-C. has been supported by Project MTM2014-57769-C3-1-P of the Spanish Ministry of Economy and Competitivity, the ERC Starting grant no. 307179 “Geometric function theory, inverse problems and fluid dynamics”, the “Ramón y Cajal” programme and the European Social Fund. X.X. acknowledges the funding by NSFC 11571354.

References

[1] A.N. Gent, P.B. Lindley, Internal rupture of bonded rubber cylinders in tension, Proc. R. Soc. Lond. Ser. A Math. Phys. Eng. Sci. 249 (1959) 195–205.
[2] C. Fond, Cavitation criterion for rubber materials: A review of void-growth models, J. Polym. Sci. B 39 (2001) 2081–2096.
[3] A. Dorfmann, Stress-softening of elastomers in hydrostatic tension, Acta Mech. 165 (2003) 117–137.
[4] S. Kundu, A.J. Crosby, Cavitation and fracture behavior of polyacrylamide hydrogels, Soft Matter 5 (2009) 3963–3968.
[5] E. Bayraktar, K. Bessri, C. Bathias, Deformation behaviour of elastomeric matrix composites under static loading conditions, Eng. Fract. Mech. 75 (9) (2008) 2695–2706.
[6] A. Cristiano, A. Marcellan, R. Long, C.-Y. Hui, J. Stolk, C. Creton, An experimental investigation of fracture by cavitation of model elastomeric networks, J. Polym. Sci. B 48 (13) (2010) 1409–1422.
[7] A.N. Gent, B. Park, Failure processes in elastomers at or near a rigid spherical inclusion, J. Mater. Sci. 19 (1984) 1947–1956.
[8] J. Michel, O. Lopez-Pamies, P. Ponte Castañeda, N. Triantafyllidis, Microscopic and macroscopic instabilities in finitely strained fiber-reinforced elastomers, J. Mech. Phys. Solids 58 (11) (2010) 1776–1803.
[9] N. Petrinic, J.L. Curiel Sosa, C.R. Siviour, B.C.F. Elliott, Improved predictive modelling of strain localisation and ductile fracture in a Ti-6Al-4V alloy subjected to impact loading, J. Phys. IV 134 (2006) 147–155.
[10] J.M. Ball, Discontinuous equilibrium solutions and cavitation in nonlinear elasticity, Philos. Trans. R. Soc. Lond. Ser. A 306 (1982) 557–611.
[11] J. Sivaloganathan, S.J. Spector, V. Tilakraj, The convergence of regularized minimizers for cavitation problems in nonlinear elasticity, SIAM J. Appl. Math. 66 (3) (2006) 736–757.
[12] D. Henao, Cavitation, invertibility, and convergence of regularized minimizers in nonlinear elasticity, J. Elasticity 94 (2009) 55–68.
[13] S. Müller, S.J. Spector, An existence theory for nonlinear elasticity that allows for cavitation, Arch. Ration. Mech. Anal. 131 (1) (1995) 1–66.
[14] J. Sivaloganathan, S.J. Spector, On the existence of minimizers with prescribed singular points in nonlinear elasticity, J. Elasticity 59 (1–3) (2000) 83–113.
[15] J. Sivaloganathan, S.J. Spector, On cavitation, configurational forces and implications for fracture in a nonlinearly elastic material, J. Elasticity 67 (1) (2002) 25–49.
[16] D. Henao, C. Mora-Corral, Invertibility and weak continuity of the determinant for the modelling of cavitation and fracture in nonlinear elasticity, Arch. Rational Mech. Anal 197 (2010) 619–655.
[17] D. Henao, C. Mora-Corral, Fracture surfaces and the regularity of inverses for BV deformations, Arch. Ration. Mech. Anal. 201 (2) (2011) 575–629.
[18] D. Henao, C. Mora-Corral, Lusin’s condition and the distributional determinant for deformations with finite energy, Adv. Calc. Var. 5 (4) (2012) 355–409.

[19] J.M. Ball, Singularities and computation of minimizers for variational problems, in: Foundations of Computational Mathematics, Oxford, 1999, in: London Math. Soc. Lecture Note Ser., vol. 284, Cambridge Univ. Press, Cambridge, 2001, pp. 1–20.
[20] J.M. Ball, G. Knowles, A numerical method for detecting singular minimizers, Numer. Math. 51 (2) (1987) 181–197.
[21] Z. Li, Element removal method for singular minimizers in variational problems involving Lavrentiev phenomenon, Proc. R. Soc. Lond. Ser. A Math. Phys. Eng. Sci. 439 (1905) (1992) 131–137.
[22] Z. Li, A numerical method for computing singular minimizers, Numer. Math. 71 (3) (1995) 317–330.
[23] Y. Bai, Z. Li, Numerical solution of nonlinear elasticity problems with Lavrentiev phenomenon, Math. Models Methods Appl. Sci. 17 (10) (2007) 1619–1640.
[24] C. Carstensen, C. Ortner, Analysis of a class of penalty methods for computing singular minimizers, Comput. Methods Appl. Math. 10 (2) (2010) 137–163.
[25] P.V. Negrón-Marrero, O. Betancourt, The numerical computation of singular minimizers in two-dimensional elasticity, J. Comput. Phys. 113 (2) (1994) 291–303.
[26] J. Bandstra, D. Koss, A simulation of growth and coalescence of voids during ductile fracture, Mat. Sci. Eng. A-Struct. 387–389 (2004) 399–403.
[27] W. Liu, X. Zhang, J. Tang, Y. Du, Simulation of void growth and coalescence behavior with 3D crystal plasticity theory, Comput. Mater. Sci. 40 (1) (2007) 130–139.
[28] S. Yerra, C. Tekoğlu, F. Scheyvaerts, L. Delannay, P. van Houtte, T. Pardoen, Void growth and coalescence in single crystals, Int. J. Solids Struct. 47 (7–8) (2010) 1016–1029.
[29] X. Xu, D. Henao, An efficient numerical method for cavitation in nonlinear elasticity, Math. Models Methods Appl. Sci. 21 (8) (2011) 1733–1760.
[30] Y. Lian, Z. Li, A numerical study on cavitation in nonlinear elasticity: defects and configurational forces, Math. Models Methods Appl. Sci. 21 (12) (2011) 2551–2574.
[31] Y. Lian, Z. Li, Position and size effects on voids growth in nonlinear elasticity, Int. J. Fract. 173 (2) (2012) 147–161.
[32] E. Roux, M. Bernacki, P. Bouchard, A level-set and anisotropic adaptive remeshing strategy for the modeling of void growth under large plastic strain, Comput. Mater. Sci. 68 (2013) 32–46.
[33] H. Kabaria, A.J. Lew, B. Cockburn, A hybridizable discontinuous Galerkin formulation for non-linear elasticity, Comp. Methods Appl. Mech. Engrg. 283 (1) (2015) 303–329.
[34] C. Su, Z. Li, Error analysis of a dual-parametric bi-quadratic FEM in cavitation computation in elasticity, SIAM J. Numer. Anal. 53 (3) (2015) 1629–1649.
[35] L. Cheng, T. Guo, Void interaction and coalescence in polymeric materials, Int. J. Solids Struct. 44 (6) (2007) 1787–1808.
[36] A. Weck, J. Segurado, J. LLorca, D. Wilkinson, H. Böhm, Numerical simulations of void linkage in model materials using a nonlocal ductile damage approximation, Int. J. Fracture 148 (3) (2007) 205–219.
[37] O. Lopez-Pamies, M.I. Idiart, T. Nakamura, Cavitation in elastomeric solids: I—A defect-growth theory, J. Mech. Phys. Solids 59 (2011) 1464–1487.
[38] O. Lopez-Pamies, T. Nakamura, M.I. Idiart, Cavitation in elastomeric solids: II—Onset-of-cavitation surfaces for Neo–Hookean materials, J. Mech. Phys. Solids 59 (2011) 1488–1505.
[39] V. Lefèvre, K. Ravi-Chandar, O. Lopez-Pamies, Cavitation in rubber: an elastic instability or a fracture phenomenon? Int. J. Fract. 192 (2015) 1–23.
[40] J. Sivaloganathan, S.J. Spector, On the optimal location of singularities arising in variational problems of nonlinear elasticity, J. Elasticity 58 (3) (2000) 191–224.
[41] A. Siddiq, R. Arciniega, T. El Sayed, A variational void coalescence model for ductile metals, Comput. Mech. 49 (2) (2012) 185–195.
[42] G. Potirniche, J. Hearndon, M. Horstemeyer, X. Ling, Lattice orientation effects on void growth and coalescence in fcc single crystals, Int. J. Plast. 22 (5) (2006) 921–942.
[43] S. Ha, K. Kim, Void growth and coalescence in f.c.c. single crystals, Int. J. Mech. Sci. 52 (7) (2010) 863–873.
[44] E.T. Seppälä, J. Belak, R.E. Rudd, Three-dimensional molecular dynamics simulations of void coalescence during dynamic fracture of ductile metals, Phys. Rev. B 71 (2005) 064112.
[45] G. Potirniche, M. Horstemeyer, G. Wagner, P. Gullett, A molecular dynamics study of void growth and coalescence in single crystal nickel, Int. J. Plast. 22 (2) (2006) 257–278.
[46] E. Lin, L. Niu, H. Shi, Z. Duan, Molecular dynamics study on the nano-void growth and coalescence at grain boundary, Sci. China-Phys. Mech. Astron. 55 (1) (2012) 86–93.
[47] C. Mi, D.A. Buttry, P. Sharma, D.A. Kouris, Atomistic insights into dislocation-based mechanisms of void growth and coalescence, J. Mech. Phys. Solids 59 (9) (2011) 1858–1871.
[48] A.A. Benzerga, J.-B. Leblond, Ductile fracture by void growth to coalescence, Adv. Appl. Mech. 44 (2010) 169–305.
[49] G.A. Francfort, J.-J. Marigo, Revisiting brittle fracture as an energy minimization problem, J. Mech. Phys. Solids 46 (8) (1998) 1319–1342.
[50] D. Henao, C. Mora-Corral, X. Xu, Γ-convergence approximation of fracture and cavitation in nonlinear elasticity, Arch. Ration. Mech. Anal. 216 (3) (2015) 813–879.
[51] L. Ambrosio, V.M. Tortorelli, Approximation of functionals depending on jumps by elliptic functionals via Γ-convergence, Comm. Pure Appl. Math. 43 (8) (1990) 999–1036.
[52] B. Bourdin, G.A. Francfort, J.-J. Marigo, Numerical experiments in revisited brittle fracture, J. Mech. Phys. Solids 48 (4) (2000) 797–826.
[53] G. Del Piero, G. Lancioni, R. March, A variational model for fracture mechanics: numerical experiments, J. Mech. Phys. Solids 55 (12) (2007) 2513–2537.
[54] S. Burke, C. Ortner, E. Süli, An adaptive finite element approximation of a variational model of brittle fracture, SIAM J. Numer. Anal. 48 (3) (2010) 980–1012.

[55] A.L. Gurson, Continuum theory of ductile rupture by void nucleation and growth: Part I—Yield criteria and flow rules for porous ductile media, J. Eng. Mater. Technol. 99 (1977) 2–15.
[56] V. Tvergaard, Material failure by void growth and coalescence, in: Advances in Applied Mechanics, Academic Press, San Diego, 1990, pp. 83–151.
[57] C. Reina, B. Li, K. Weinberg, M. Ortiz, A micromechanical model of distributed damage due to void growth in general materials and under general deformation histories, Int. J. Num. Methods Engrg. 93 (6) (2013) 575–611.
[58] L. Fokoua, S. Conti, M. Ortiz, Optimal scaling in solids undergoing ductile fracture by void sheet formation, Arch. Ration. Mech. Anal. 212 (2014) 331–357.
[59] L. Fokoua, S. Conti, M. Ortiz, Optimal scaling laws for ductile fracture derived from strain-gradient microplasticity, J. Mech. Phys. Solids 62 (2014) 295–311.
[60] S. Heyden, B. Li, K. Weinberg, S. Conti, M. Ortiz, A micromechanical damage and fracture model for polymers based on fractional strain-gradient elasticity, J. Mech. Phys. Solids 74 (2015) 175–195.
[61] J.M. Ball, Convexity conditions and existence theorems in nonlinear elasticity, Arch. Ration. Mech. Anal. 63 (1977) 337–403.
[62] J.M. Ball, Some open problems in elasticity, in: Geometry, Mechanics, and Dynamics, Springer, New York, 2002, pp. 3–59.
[63] S. Müller, Det = det. A remark on the distributional determinant, C. R. Acad. Sci., Paris I 311 (1) (1990) 13–17.
[64] D. Mumford, J. Shah, Optimal approximations by piecewise smooth functions and associated variational problems, Comm. Pure Appl. Math. 42 (1989) 577–685.
[65] L. Ambrosio, N. Fusco, D. Pallara, Functions of Bounded Variation and Free Discontinuity Problems, Oxford University Press, New York, 2000.
[66] A.A. Griffith, The phenomena of rupture and flow in solids, Philos. Trans. R. Soc. Lond. Ser. A 221 (1921) 163–198.
[67] L. Ambrosio, V.M. Tortorelli, On the approximation of free discontinuity problems, Boll. Unione Mat. Ital. B (7) 6 (1) (1992) 105–123.
[68] M. Focardi, On the variational approximation of free-discontinuity problems in the vectorial case, Math. Models Methods Appl. Sci. 11 (4) (2001) 663–684.
[69] A. Braides, A. Chambolle, M. Solci, A relaxation result for energies defined on pairs set-function and applications, ESAIM Control Optim. Calc. Var. 13 (4) (2007) 717–734.
[70] M. Crouzeix, P.-A. Raviart, Conforming and nonconforming finite element methods for solving the stationary Stokes equations I, Rev. Française Automat. Informat. Recherche Opérationnelle Sér. Rouge 7 (R3) (1973) 33–75.
[71] P.G. Ciarlet, The finite element method for elliptic problems, in: Studies in Mathematics and its Applications, Vol. 4, North-Holland Publishing Co., Amsterdam, 1978.
[72] A.E. Oberth, R.S. Bruenner, Tear phenomena around solid inclusions in castable elastomers, Trans. Soc. Rheol. 9 (1965) 165–185.
[73] R. Stringfellow, R. Abeyaratne, Cavitation in an elastomer: Comparison of theory with experiment, Mat. Sci. Engrg. A 112 (1989) 127–131.
[74] S. Müller, Q. Tang, B.S. Yan, On a new class of elastic deformations not allowing for cavitation, Ann. Inst. H. Poincaré Anal. Non Linéaire 11 (2) (1994) 217–243.
[75] P.G. Ciarlet, Mathematical elasticity. Vol. I, in: Studies in Mathematics and its Applications, vol. 20, North-Holland Publishing Co., Amsterdam, 1988.
[76] L.C. Evans, R.F. Gariepy, Measure Theory and Fine Properties of Functions, CRC Press, Boca Raton, FL, 1992.
[77] L.C. Evans, Partial differential equations, in: Graduate Studies in Mathematics, Vol. 19, American Mathematical Society, Providence, RI, 1998.
[78] R. Adams, Sobolev Spaces, Academic Press, New York, 1975.
[79] D. Henao, S. Serfaty, Energy estimates and cavity interaction for a critical-exponent cavitation model, Comm. Pure Appl. Math. 66 (2013) 1028–1101.